



Article

# From Flat Plates to Sinusoidal Structures: Influence of Geometry on the Energy Absorption Capability of Carbon/Epoxy Composites

Mehmet Engül \* and Nuri Ersoy

Department of Mechanical Engineering, Boğaziçi University, Istanbul 34342, Turkey

\* Correspondence: mehmet.engul@boun.edu.tr

**Abstract:** Composite structures have excellent performance related to energy absorption during crush events. Among various factors, geometry has a significant influence on the specific energy absorption (SEA) performance of composites; however, the variation of crush-induced failure mechanisms for various geometric features and the way they affect energy absorption capability have not yet been fully clarified. Moving from simple to complex composite structures, a holistic study investigating the influence of geometry on the SEA is required. This paper presents experimental and numerical investigations of the crushing process for flat plates, semi-circle geometries, and sinusoidal structures with different diameters and numbers of curvatures. In a numerical analysis, a finite element (FE) model with the idea of an artificial plug-initiator was developed for the accurate and realistic crushing behavior of sinusoidal specimens. The results were discussed and compared in terms of the observed failure mechanisms. The sinusoidal structure with the highest energy absorption capability was identified.

**Keywords:** polymer composites; sinusoidal structures; crashworthiness; FE model



**Citation:** Engül, M.; Ersoy, N. From Flat Plates to Sinusoidal Structures: Influence of Geometry on the Energy Absorption Capability of Carbon/Epoxy Composites. *J. Compos. Sci.* **2023**, *7*, 56. <https://doi.org/10.3390/jcs7020056>

Academic Editors: Marco Monti and Ilaria Armentano

Received: 24 November 2022

Revised: 9 December 2022

Accepted: 3 January 2023

Published: 3 February 2023



**Copyright:** © 2023 by the authors. Licensee MDPI, Basel, Switzerland. This article is an open access article distributed under the terms and conditions of the Creative Commons Attribution (CC BY) license (<https://creativecommons.org/licenses/by/4.0/>).

## 1. Introduction

The automotive and aerospace industries are always under pressure to meet the demands for better safety and crashworthiness performances. While collapsing in a crash event, structures should absorb impact energy in a controlled manner so that high deceleration, which causes fatal injuries, is minimized. Additionally, these structures are also expected to be lightweight to decrease fuel consumption and greenhouse gas emissions. Carbon fiber-reinforced plastic (CFRP) composites are increasingly being used for its crashworthy components in the industry because of their benefits over metallic materials, including a high strength-to-weight ratio and superior energy absorption characteristics. However, the energy absorbed by a composite structure is not easily predicted due to the complexity of the crush-induced failure mechanisms, including not only intralaminar but also interlaminar damage modes.

From the 1980s to the present, there have been extensive literature about the energy absorption of composite structures, and the view commonly shared by the researchers is that there are several different failure modes occurring simultaneously during the crush event, which can be categorized as (i) delamination, (ii) splaying (bending of delaminated layers), and (iii) fragmentation (fiber breakage and matrix cracking as the result of in-plane failure) [1–5]. Each of these failure modes provides a different capability of energy absorption. Among the limited number of studies investigating the levels of energy absorption of different failure modes, Israr et al. [6] carried out both numerical and experimental investigations of the crushing process of CFRP plates and demonstrated that the fragmentation mode occurred due to the fiber breakage absorbing more energy than the other failure types. The dominant failure mode during the crushing of composite structures depends on several factors, such as the selection of the material system, fiber orientation, the strain rate,

and trigger mechanisms, which have been the subject of many studies in the past [7–12]. Recently, interest in composite coupon-level tests is increasing, since flat plates are easy to manufacture while providing a standardization so that the energy absorption capabilities of different materials and configurations can be systematically compared [6,13,14]. Moving away from flat plates, geometry has a significant influence on the SEA, and it is especially known that corrugated designs, such as sinusoidal geometries, improve the energy absorption capability to a considerable extent. However, most of the previous studies focused on closed geometric features, such as tubular specimens [1,4,15–18], and there are a limited number of studies based on sinusoidal structures. Hanagud et al. [19] were among the first researchers to carry out experimental tests on sinusoidal specimens; they exhibited that the sinusoidal geometry has great potential in terms of energy absorption. Afterwards, Wiggenraad et al. [20] conducted a complete set of tests to understand the crashworthiness of subfloor composite sinusoidal structures designed for aerospace applications; however, the failure modes were not clearly identified, and the numerical attempts made to predict the crushing behavior were not quite successful. Sokolinsky et al. [21] then estimated the crushing response of carbon/epoxy-corrugated sinusoidal plates accurately by applying a numerical simulation in Abaqus/Explicit. However, this study focused only on the validation of the numerical analysis, with the experimental data obtained from one specific geometry. There was no discussion about the failure modes occurring during the crushing process and how these modes affected the energy absorption capability of the structure. It can be concluded that, among the numerous studies focusing on the crashworthiness of different composite geometries, there has been no work conducting a systematic study to understand the influence of geometry on energy absorption capability, starting from flat plates to complex structures. Moreover, the change of failure modes with different geometries and the relationship between these modes and the amount of absorbed energy are still unclear.

In this paper, the influence of geometry on the SEA of AS4/8552 carbon/epoxy composite structures was investigated through various geometries, such as flat-plate, semi-circle, and sinusoidal specimens. While keeping the cross-sectional area (weight) constant, sinusoidal structures with different numbers of curvatures and diametral sizes were tested, and their energy absorption capabilities were compared. In addition to experimental tests, a finite element (FE) model was developed in Abaqus/Explicit for sinusoidal structures to estimate the SEA numerically. Advances in commercial finite element analysis (FEA) software have enabled engineers to simulate the performance of composite components; however, the crushing behavior and the failure mechanisms cannot always be predicted accurately. For that purpose, the idea of an artificial plug-initiator was incorporated into the FE model to obtain an accurate crushing morphology. After the numerical approach was validated, the crush simulation of another sinusoidal structure with more curvatures was presented. All results were compared in terms of the observed failure mechanisms and their contribution to the SEA values; the structure with the highest energy absorption capability was identified.

## 2. Experimental Section

### 2.1. Flat Plate

The flat-plate specimens were manufactured from Hexcel AS4/8552 carbon-epoxy UD prepregs with 198 g/m<sup>2</sup> areal weights. The manufacturing process was carried out in an autoclave according to the manufacturer's recommended cure cycle [22]. During the manufacturing process, 8 plies of prepregs were stacked with a [0/90]<sub>2s</sub> cross-ply configuration on the flat, steel mold. The 300 mm × 300 mm plates thus manufactured were then cut using a diamond disk cutter into test coupons, with a 56 mm length, 20 mm width, 1.47 mm thickness, and 45° chamfered edge. Chamfered edges were polished and inspected visually to ensure that the cutting operation did not cause any delamination.

A simple fixture with a 50 mm length was designed to provide a supporting system. The illustration of the fixture, the specimen, and the test setup are demonstrated in Figure 1.

The unsupported length was specified as 6 mm, which was suitable to prevent the specimen from buckling. Three specimens were tested in a Zwick Z100 testing machine, with a quasi-static speed of 0.5 mm/min. The tests were ended manually before the crushing plate compressed the specimen fixture. The load was measured with a 100 kN load cell, and the displacement was measured from the crosshead movement of the testing machine.

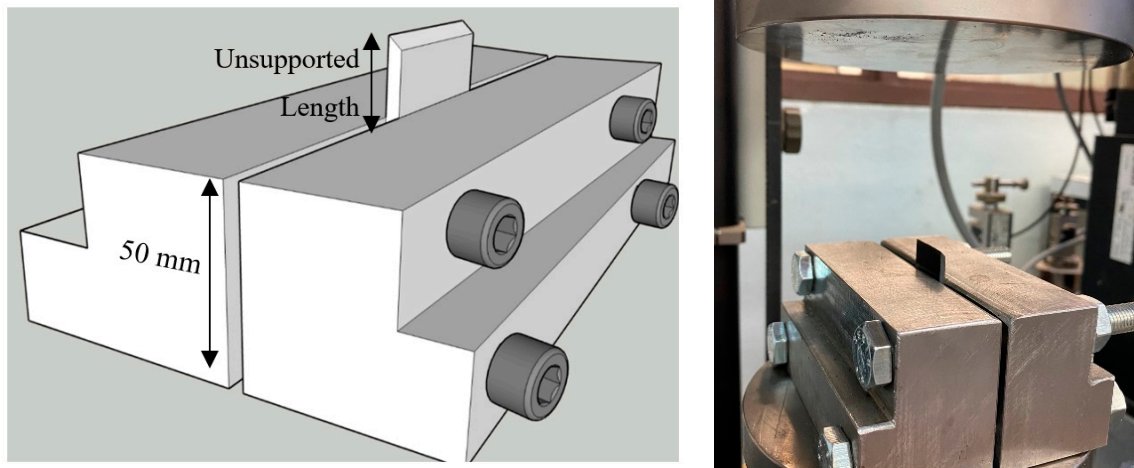


**Figure 1.** The illustration of the flat-plate specimen with the supporting fixture (left) and the test setup (right).

## 2.2. Semi-Circle Structure

The semi-circle specimens were manufactured from Hexcel AS4/8552 carbon-epoxy UD prepregs by using the same technique as the flat plates. A total of 8 plies of prepregs were stacked on the custom design mold, with a  $[0/90]_{2s}$  cross-ply configuration. The schematic of the cross-section is shown in Figure 2. The cross-section of the structure had a semi-circle with a 45 mm radius and 8 mm straight lines positioned at each end-lip for extra stability.

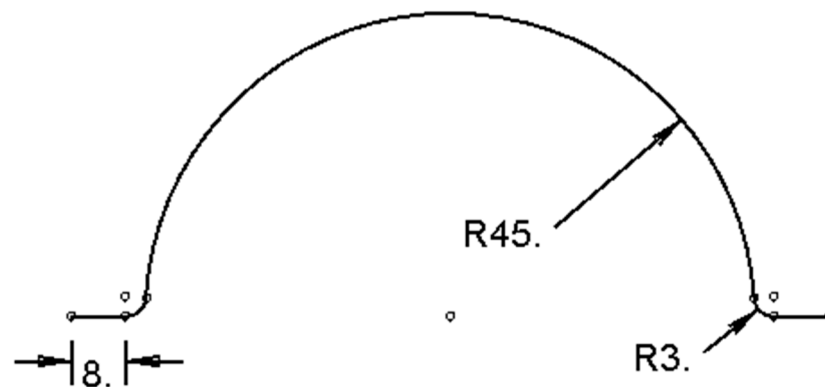


**Figure 2.** The schematic of the cross-section of the semi-circle specimen. (All dimensions are given in millimeters.)

Specimens again had a 1.47 mm thickness and a 56 mm length. A 45° chamfer was also applied to one edge of the specimens to avoid catastrophic failure and to decrease the peak load. Three specimens were tested in the Zwick Z100 testing machine, with a quasi-static speed of 0.5 mm/min. The tests were ended after the displacement of the crushing plate reached 20 mm and the load-displacement curves were obtained.

### 2.3. Sinusoidal Structures

The design of the sinusoidal structures consisted of different numbers of repeating semi-circle curvatures. The idea was to keep the amount of material (weight) constant while adding more semi-circle curvatures, which would lead to a decrease in the radii. Therefore, the sinusoidal structures with 3 curvatures (with 15 mm radii) and with 5 curvatures (with 9 mm radii) were designed and manufactured. Both structures had 8 mm straight lines positioned at each end-lip, which was the same as the semi-circle specimens. The schematics of the cross-sections of the sinusoidal structures with 3 and 5 curvatures can be seen in Figure 3.

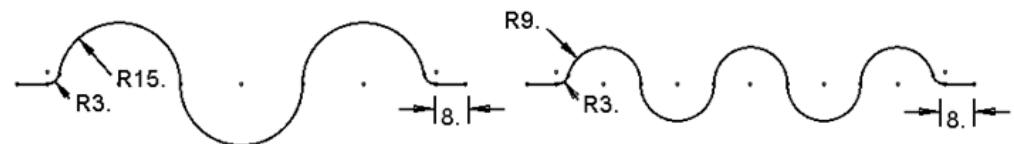


**Figure 3.** The schematic of the cross-sections of the sinusoidal structures with 3 curvatures (**left**) and 5 curvatures (**right**). (All dimensions are given in millimeters.)

The manufacturing process was carried out in an autoclave by stacking 8 plies of AS4/8552 carbon-epoxy UD prepregs on the custom design molds, with a  $[0/90]_{2s}$  configuration. Three specimens with a 56 mm length were tested for their geometries by applying the same testing conditions as the previous samples. Figure 4 shows the semi-circle and sinusoidal test specimens with 3 and 5 curvatures.

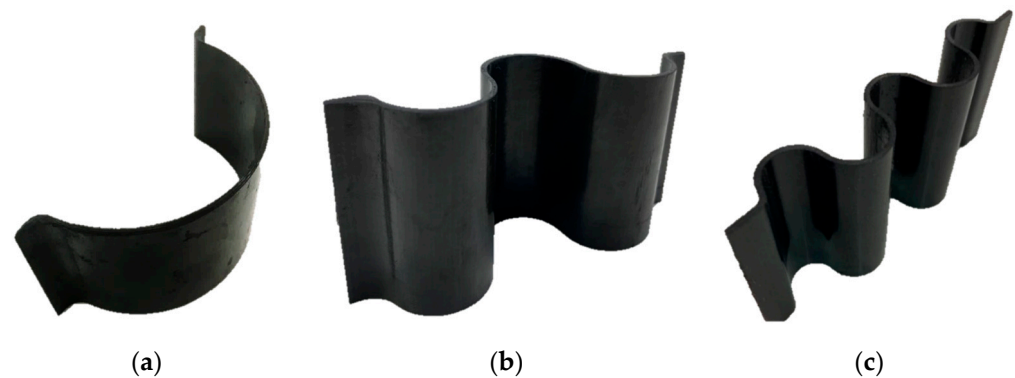


**Figure 4.** Manufactured semi-circle (a) and sinusoidal specimens with 3 (b) and 5 curvatures (c).

## 3. Numerical Model

### 3.1. Validation

In addition to sinusoidal structures with three and five semi-circle curvatures, for a deeper understanding of the influence of geometry on the SEA, the crushing of the sinusoidal structure with seven curvatures required investigation. This part of the study was carried out with numerical analysis only for two main purposes: to develop an FE Model, which can predict the energy absorption capability of complex structures with accurate crushing behavior, and to decrease the manufacturing cost. Before that stage, the FE model should be validated by using the sinusoidal structures with three and five curvatures, of which experimental data has already been obtained.

The FE model for the progressive damage of AS4/8552 carbon fiber/epoxy sinusoidal structures with three and five curvatures were developed in Abaqus/Explicit while considering both the intralaminar (in-plane) and interlaminar (delamination) damage mechanisms. Half of the geometry was modeled by applying symmetry conditions. Each of the eight plies were individually extruded and meshed with continuum shell elements (SC8R). Continuum shell elements in ABAQUS have the geometry of a three-dimensional solid element, but their kinematic and constitutive behaviors are similar to those of conventional

shell elements. Boundary conditions were applied to be coherent with the experimental procedure. The Abaqus/CAE model can be seen in Figure 5.

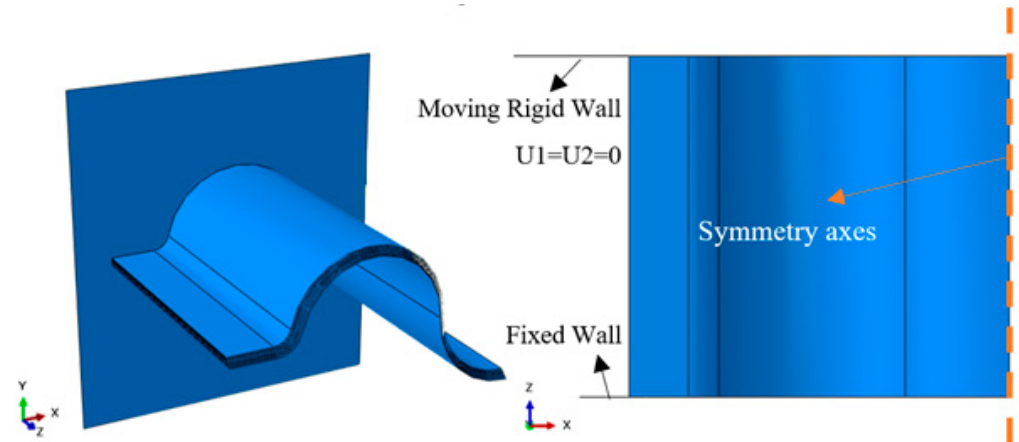


**Figure 5.** Abaqus/CAE half model of the sinusoidal structure with 3 curvatures: isometric view (**left**) and front view (**right**).

The in-plane response of the composite plies was modeled according to the Hashin damage criteria [23] as a homogeneous orthotropic material, which is capable of sustaining progressive stiffness degradation due to fiber/matrix cracking. The failure initiation criteria [23] can be demonstrated as:

$$\text{Tensile fiber failure for } \sigma_{11} \geq 0 \quad \left(\frac{\sigma_{11}}{X_T}\right)^2 + \alpha\left(\frac{\sigma_{12}}{S}\right)^2 \geq 1 \quad (1)$$

$$\text{Compressive fiber failure for } \sigma_{11} < 0 \quad \left(\frac{\sigma_{22}}{X_C}\right)^2 \geq 1 \quad (2)$$

$$\text{Tensile matrix failure for } \sigma_{22} > 0 \quad \left(\frac{\sigma_{22}}{Y_T}\right)^2 + \alpha\left(\frac{\sigma_{12}}{S}\right)^2 \geq 1 \quad (3)$$

$$\text{Compressive matrix failure for } \sigma_{22} < 0 \quad \left(\frac{\sigma_{22}}{2S}\right)^2 + \left[\left(\frac{Y_C}{2S}\right)^2 - 1\right] \frac{\sigma_{22}}{Y_C} + \left(\frac{\sigma_{12}}{S}\right)^2 \geq 1 \quad (4)$$

where  $\sigma_{11}$  and  $\sigma_{22}$  are normal stresses in fiber and transverse directions, while  $\sigma_{12}$  symbolizes shear stress;  $X_T$  and  $X_C$  are fiber direction tensile and compressive strength values;  $Y_T$  and  $Y_C$  are transverse tensile and compressive strengths; and  $S$  symbolizes shear strength. The behavior of the material after damage onset was determined by the damage evolution that was characterized by the degradation of material stiffness. The response of the material was computed from:

$$C_d = \frac{1}{D} \begin{bmatrix} (1-d_1)E_{11} & (1-d_1)(1-d_2)v_{21}E_{11} & 0 \\ (1-d_1)(1-d_2)v_{12}E_{22} & (1-d_2)E_{22} & 0 \\ 0 & 0 & (1-d_{12})G_{12}D \end{bmatrix} \quad (5)$$

where  $D = 1 - (1-d_1)(1-d_2)v_{12}v_{21}$ ;  $E_{11}$  and  $E_{22}$  are Young’s modulus in fiber and transverse directions;  $G_{12}$  is the shear modulus; and  $v_{12}$  and  $v_{21}$  denote the Poisson’s ratios. The symbols  $d_1$ ,  $d_2$ , and  $d_{12}$  represent the current state of fiber, matrix, and shear damages. In the progressive damage algorithm of Abaqus, even if one type of damage is completed, the element is not deleted unless all other damage variables reach 1. This damaged but not deleted element can still bear some load; however, they have a mostly negligible effect on energy absorption capability. On the other hand, the influence of these elements on the crushing morphology during the deformation can be an issue to overcome.

Other than in-plane failure, delamination is another predominant mode of failure, especially under axial loading. In the case of axial crash, instead of single mode, mixed-mode delamination occurred, which contained opening and shearing modes. Therefore, it was necessary to apply a general formulation dealing with mixed-mode delamination onset and propagation [24]. Camanho et al. [25] proposed a cohesive zone model (CZM) in which the interactions between plies were developed, which can capture delamination initiation and progress under mixed-mode conditions. In this model, cohesive surfaces were defined, which utilized the relation between tractions and separations. The damage initiation was calculated using the quadratic formula given in Equation (6). The linear softening damage law was used for the cohesive damage softening, with the mixed-mode fracture energy criteria based on power law (Equation (7)).

$$\left(\frac{\sigma_I}{\tau_I}\right)^2 + \left(\frac{\sigma_{II}}{\tau_{II}}\right)^2 + \left(\frac{\sigma_{III}}{\tau_{III}}\right)^2 = 1 \tag{6}$$

$$\left(\frac{G_I}{G_I^c}\right)^\alpha + \left(\frac{G_{II}}{G_{II}^c}\right)^\alpha + \left(\frac{G_{III}}{G_{III}^c}\right)^\alpha = 1 \tag{7}$$

where  $\tau_I$ ,  $\tau_{II}$ , and  $\tau_{III}$  are interfacial strength values of Mode I, Mode II, and Mode III;  $G_I^c$  is the normal fracture toughness;  $G_{II}^c$  and  $G_{III}^c$  are shear fracture toughness values for Mode II and Mode III, respectively;  $G_I$  is the normal strain energy release rate; and  $G_{II}$  and  $G_{III}$  are shear strain energy release rates for Mode II and Mode III, respectively. The desired interlaminar properties for 1 mm mesh size were extrapolated, as suggested in the study of Turon et al. [26]. According to this study, there should be a minimum of 4–5 elements in the cohesive zone (the area from the point of maximum traction to the crack tip) to achieve accurate delamination behavior; the suggested process is to decrease the interfacial strength values artificially to increase the cohesive zone length so that larger elements can be utilized. The input properties required both in-plane and interlaminar failure for the 1 mm mesh size are listed in Table 1 [22,27–29].

**Table 1.** The material properties of AS4/8552 composite [22,27–29].

Description	Unit	Variable	Value
Density	g/cm <sup>3</sup>	$\rho$	1.58
Longitudinal Modulus	GPa	$E_{11}$	141
Transverse Modulus	GPa	$E_{22} = E_{33}$	9.75
Principal Poisson’s Ratio	-	$\nu_{12}$	0.267
Shear Moduli in 1–2 Plane	GPa	$G_{12} = G_{13}$	5.2
Shear Moduli in 2–3 Plane	GPa	$G_{23}$	3.19
Longitudinal Tensile Strength	MPa	$X_T$	2200
Longitudinal Compressive Strength	MPa	$X_C$	1500
Transverse Tensile Strength	MPa	$Y_T$	81
Transverse Compressive Strength	MPa	$Y_C$	260
In-plane Shear Strength	MPa	$S$	80
Interfacial Strength (Mode I)	MPa	$\tau_I$	35
Interfacial Strength (Modes II and III)	MPa	$\tau_{II} = \tau_{III}$	70
Fracture Toughness (Normal)	[kJ/mm <sup>2</sup> ]	$G_I^c$	0.28
Fracture Toughness (Shear)	[kJ/mm <sup>2</sup> ]	$G_{II}^c = G_{III}^c$	2.59

The velocity of the rigid upper wall was defined as 200 mm/s. A higher value of velocity than the quasi-static test speed was utilized in the simulation in order to reduce step time, which led to a low computational cost. Since dynamic effects become important when the velocity is higher than 500 mm/s, this amount of artificial increase had no significant influence on the simulation results [21]. The friction between the composite specimen and the rigid upper wall played a significant role in finite element analysis. The friction coefficient was taken to be 0.3, as suggested in Ref. [21]. Moreover, to achieve reasonable run times, mass scaling with the factor of 10<sup>2</sup> was applied. Mass scaling is a technique that

artificially increases the mass of the structure to obtain a larger time step, which leads to lower run times [30]. The simulation of the sinusoidal structure with three curvatures took 145 min of run time on a 16-core workstation.

### 3.2. The Idea of Artificial Plug-Initiator

One of the purposes of this study was to correlate the crushing behavior of the structures in the numerical analysis with the actually observed modes. As will be elaborated in the results section, although the numerical results showed good agreement with the experimental data in terms of load-displacement curves, there were some mismatches that occurred between the observed failure modes and the simulated crushing morphology. At that point, the idea of using an artificial plug-initiator in the finite element model was proposed to initiate delamination properly and create a V-shaped area to simulate the debris wedge formation during testing. Various geometries were designed and implemented in the FE model, and Figure 6 demonstrates the final shape of the artificial plug-initiator, presenting the most accurate results. The different attempts made for the plug-initiator design and their influences on numerical results are presented in the results section.

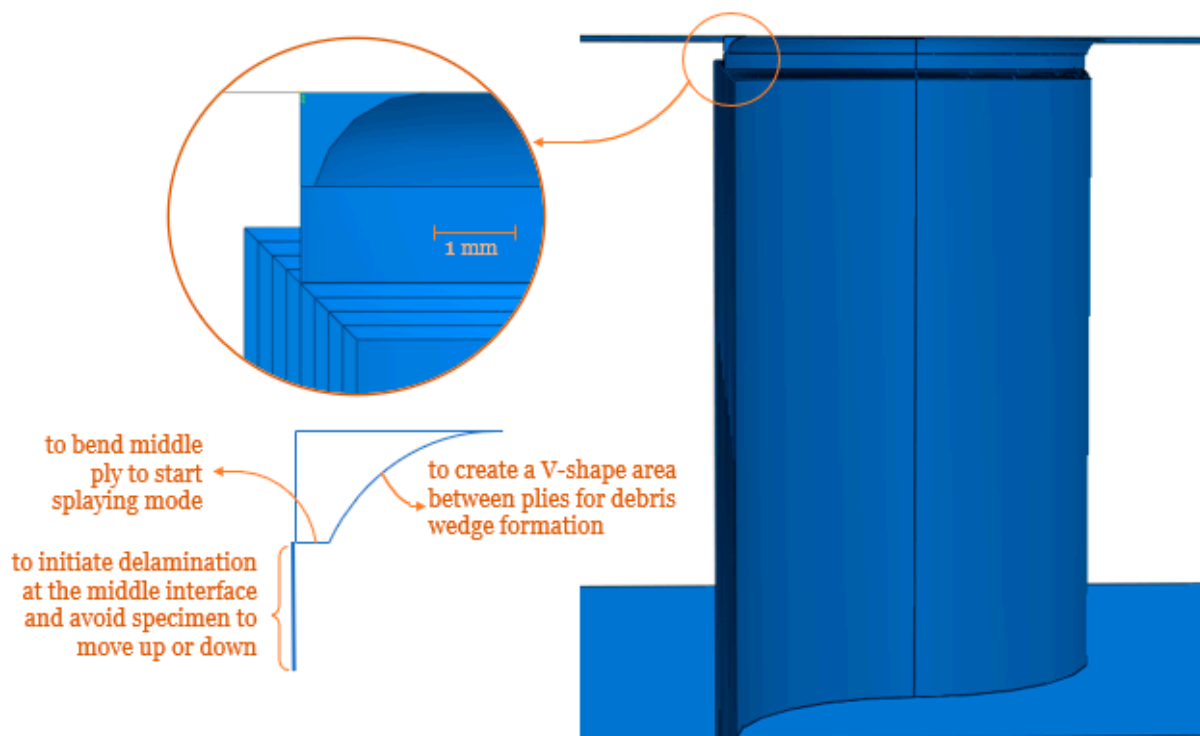


**Figure 6.** The finalized version of the artificial plug-initiator design with the position in assembly.

### 3.3. Sinusoidal Structure with 7 Curvatures

The validated FE model in Abaqus/Explicit was then applied to the AS4/8552 carbon fiber/epoxy sinusoidal structures with seven curvatures by modeling half of the geometry to benefit from the symmetry conditions. Since the amount of material was desired to be the same as previous geometries, the radius of the repeating semi-circle segments was determined to be 6.43 mm. The schematic of the cross-section and the Abaqus/CAE half model is presented in Figure 7. The simulation of the 10 mm crush took 244 min of run time on a 16-core workstation.

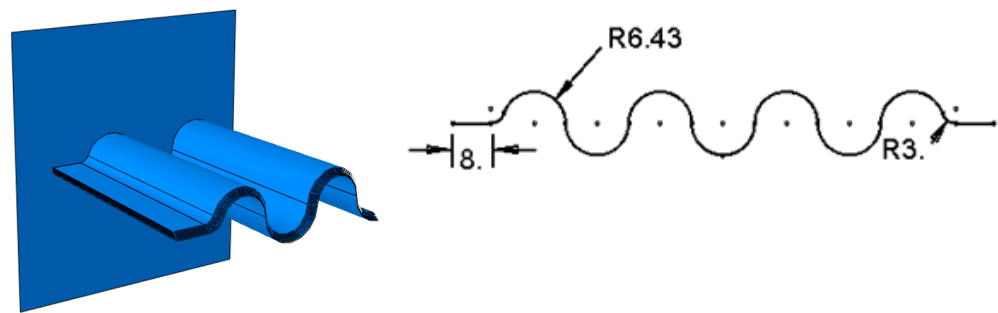


**Figure 7.** Abaqus/CAE model (right) and the schematic of the mid-plane of sinusoidal structures with 7 curvatures (left). (All dimensions are given in millimeters.)

## 4. Results and Discussion

### 4.1. Experimental Results of Flat Plate

The first step of the experimental study was to understand the load-displacement trend of the flat plates and failure mechanisms, which resulted in the experimentally observed crushing morphology. Figure 8 presents the load-displacement curves of flat plates with eight plies, obtained from the quasi-static compression tests, and a snapshot taken during the tests.

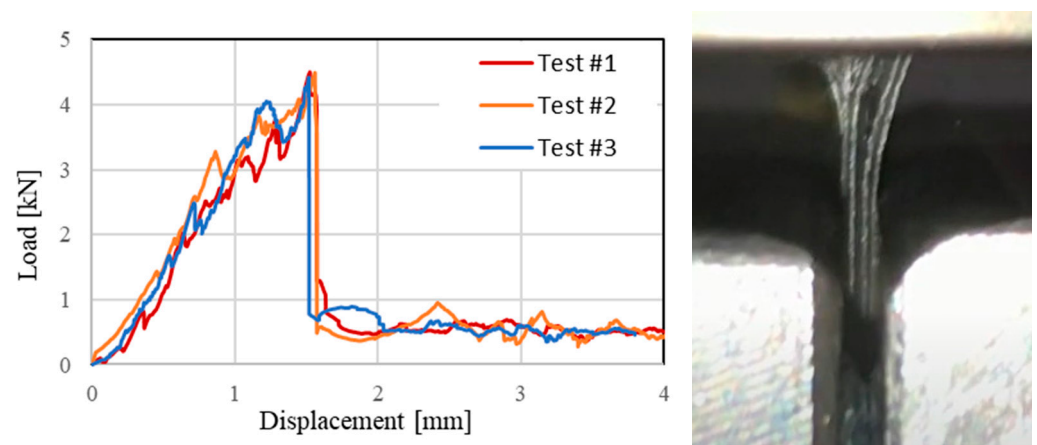


**Figure 8.** The results of the flat specimens: load-displacement curve (left) and deformed shape (right).

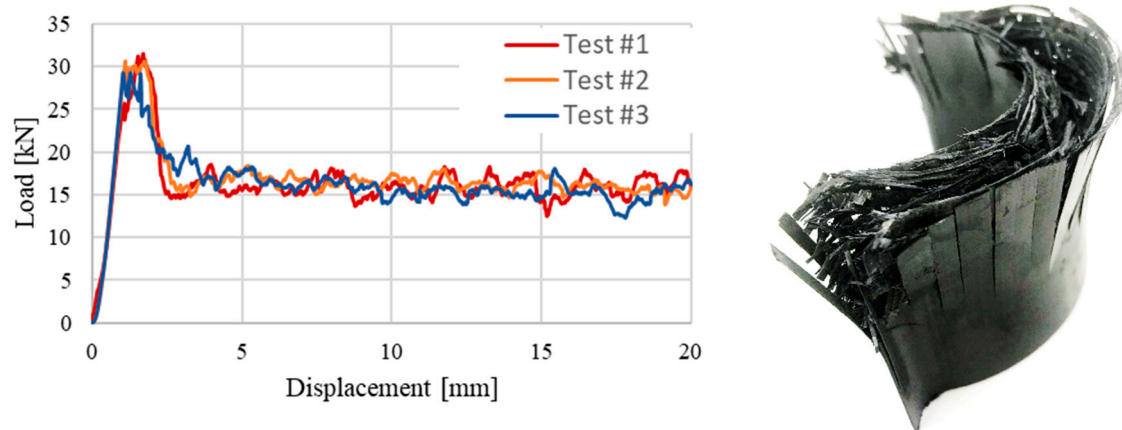
According to the observations made from the crushing morphology of the flat specimen, at the beginning of the process, delamination started at the interface between the first and second plies, due to the high stress levels at the tip of the chamfer. After that point, the first ply, subjected to the axial load by the moving rigid wall, started to bend, and that created the splaying mode. In a cross-ply specimen, 0-degree plies generally have a higher tendency to bend; therefore, fiber tensile failures can be seen, due to the bending mode. After some plies were splayed, fragmentation occurred at the plies that did not bend or splay. The fragmentation mode was characterized by two types of failure. The first type was matrix cracking, occurring in the 90-degree plies due to shear. The second type was fiber failure in the 0-degree plies, located in the center, due to the micro-buckling of the fibers. After delamination had initiated at all seven interfaces, the load reached its peak level. A stable zone started after about a 1.5 mm crush, where the load fluctuated around a mean load, and the main failure modes were micro-fragmentation and splaying. Specific energy absorption (SEA), which is the energy obtained from the area under the load-displacement curve per crushed mass, was calculated, as can be seen from Table 2.

**Table 2.** SEA values of flat-plate specimens.

Specimen No.	SEA [J/g]	Average
#1	32.31	32.14
#2	32.18	
#3	31.94	

#### 4.2. Experimental Results of Semi-Circle Specimens

Figure 9 demonstrates the load-displacement curves of three semi-circle specimens tested under quasi-static compression together with the crushing morphology of the first specimen. The SEA value for each specimen was calculated from the division of the area under the curve by the crushed weight, and the average of the results was evaluated to be 48.09 J/g (see Table 3). The reason behind the increase in energy absorption capability by approximately 50% when compared to flat specimens can be explained by the change of failure mechanisms. During the crushing process, in addition to the splaying of the 0-degree plies, vertical ruptures occurred, which are characterized by long matrix cracks. Moreover, the level of fragmentation increased in the plies located near the center, which automatically led to a higher amount of energy absorption.

**Figure 9.** The results of the semi-circle specimens: load-displacement curve (left) and the deformed shape (right).**Table 3.** SEA values of semi-circle specimens.

Specimen No	SEA [J/g]	Average
#1	48.22	48.09
#2	48.94	
#3	47.12	

#### 4.3. Experimental Results of Sinusoidal Specimens

The deformed shapes of the sinusoidal structures with three and five curvatures are given in Figure 10. According to the observations made during the tests, it can be said that the reflection points in the sinusoidal structure, which connected the repeating semi-circle segments to another, created obstacles that made the splaying of the plies more difficult. Therefore, more micro-buckling occurred in 0-degree plies, resulting in fiber breakage, and more matrix cracks were initiated in the 90-degree plies located at the center. Moreover, for the sinusoidal structure with three curvatures, the number of vertical ruptures occurring at the outer plies increased when compared to the semi-circle specimen. This number became much higher for the sinusoidal structure with five curvatures. These observations led to the

conclusion that sinusoidal structures have better performance in terms of energy absorption. The load displacement curves (see Figure 11) and the SEA results evaluated from these curves (see Table 4) confirmed this conclusion. Sinusoidal structures with five curvatures absorbed more energy than the others.



Figure 10. The deformed shapes of the sinusoidal specimens with 3 (left) and 5 curvatures (right).

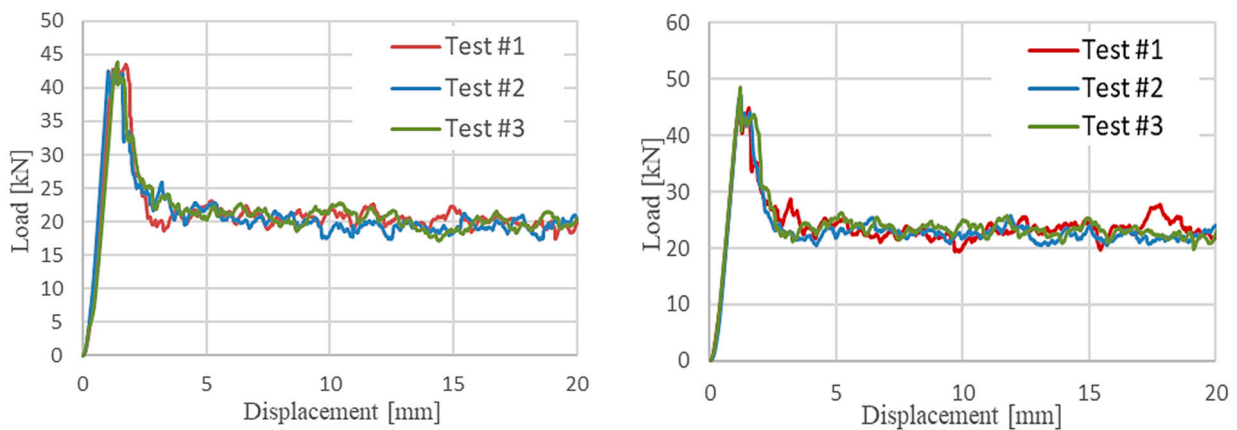


Figure 11. Load-displacement curves of the sinusoidal specimens with 3 (left) and 5 curvatures (right).

Table 4. SEA values of the semi-circle specimens.

Number of Curvatures	Specimen No	SEA [J/g]	Average
3	#1	62.71	62.64
	#2	62.18	
	#3	63.03	
5	#1	69.01	68.73
	#2	68.24	
	#3	68.94	

A question arose at that point: “For sinusoidal structures having more curvatures than 5, will there be a limit where an asymptotic trend in SAE is observed?” To answer this question, as further investigation, the numerical analysis for the crushing process of the sinusoidal structure with seven curvatures was performed, and the results are presented in the next section.

#### 4.4. Numerical Results

The FE model was developed for the progressive damage of AS4/8552 carbon fiber/epoxy sinusoidal structures with three curvatures, and the comparison between the load-displacement and energy curves of the experimental and numerical studies is presented in Figure 12. Although there were some fluctuations in the load-displacement curve obtained from the numerical study, the overall trend was similar to the experimental data, and more importantly, the model was able to predict the amount of energy absorbed during the crushing process accurately. In this model, the slight kink in the energy-displacement curve corresponded to the point where the crush zone reached the end of the chamfer, after which the energy absorption uniformly increased as the crush zone proceeded.

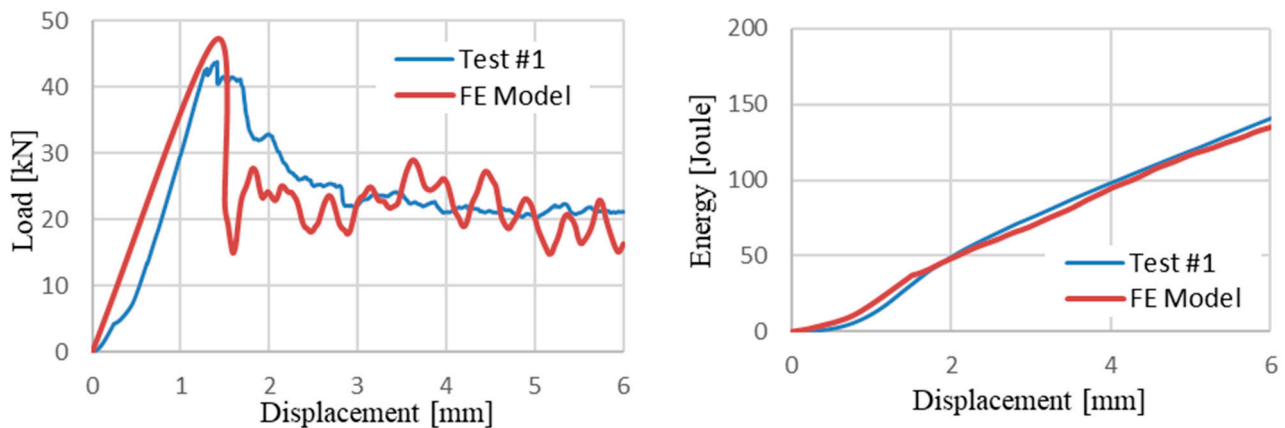


**Figure 12.** Comparison of the FE model of the sinusoidal specimen with 3 curvatures using experimental tests: load-displacement curves (left) and energy curves (right).

The main problem posed in the model, however, was that it was unable to simulate the crushing behavior and corresponding failure mechanisms correctly. Figure 13 shows the deformed shape at the end of the simulation when the displacement was 6 mm. As can be seen from the right side of the figure, which demonstrates the cross-sectional view from the middle of the specimen, instead of the splaying of the outer plies and the micro-buckling in the inner plies, a global buckling occurred, which led to a catastrophic failure. Due to the excessive distortion, the model was aborted at a crush distance of 6 mm and did not proceed. Even though the simulated crushing behavior was different from the experimentally observed one, it is interesting that the FE model can still estimate the SEA of the composite structure accurately. The reason behind this can be explained by the repartition of the energy balance during the process. During the early stages of deformation, although the order of occurrence and the distribution of damage modes differed from experimentally observed ones, the overall energy absorbed by those damage modes was consistent with the actual data. However, the main problem arose after some level of deformation, when the damage mode changed dramatically, and catastrophic failure occurred due to local buckling, which terminated the model. Therefore, an artificial plug-initiator was introduced into the simulation to provide an accurate FE model, in which damage modes can occur in the correct order and levels.

During the numerical study, various geometries for the plug-initiator were designed and tried within the FE model. The purpose behind including the plug-initiator in the FE model was to simulate the experimentally observed splaying mode and to create a V-shaped separation between the delaminated plies, which leads debris formation, as occurred in the actual tests. Figure 14 shows three types of plug initiators and their corresponding simulation results to show the evaluation of the damage. As can be seen from the figure, with the type-III plug-initiator, the FE model showed consistency in terms of the crushing morphology observed experimentally. Simulation results showed that the model was

successful in demonstrating the failure mechanisms accurately when compared with the actual tests. The numerical model can predict the specimen behavior consistently, without global buckling and excessive distortion (see Figure 15). Moreover, in Figure 16, matrix crack growth at the outer plies and the delamination growth at the first interface was presented step by step, which was also consistent with the actual damage progression.

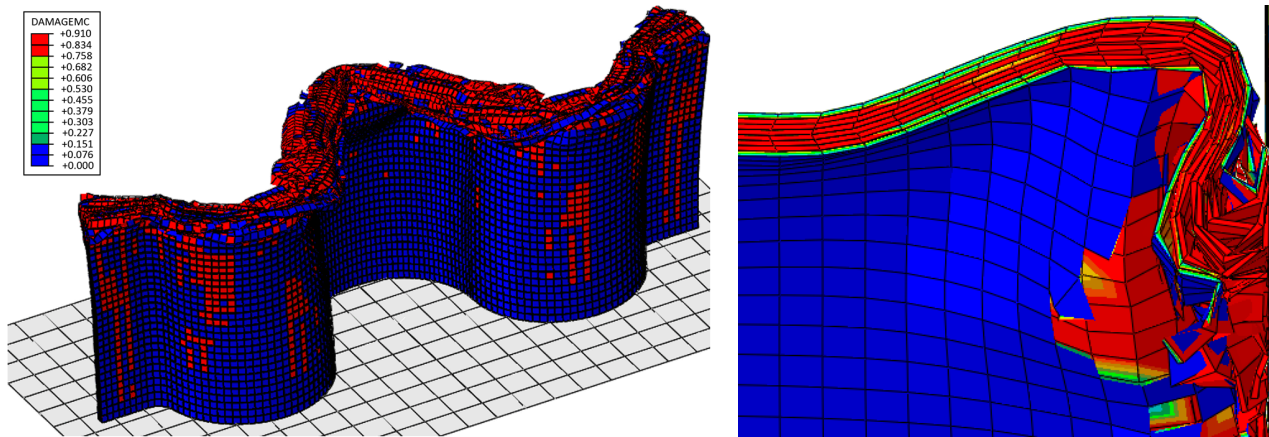


**Figure 13.** Simulated deformed shapes of the sinusoidal specimen with 3 curvatures: isometric view with demonstrated matrix failure (**left**) and cross-sectional view from the mid-plane (**right**).

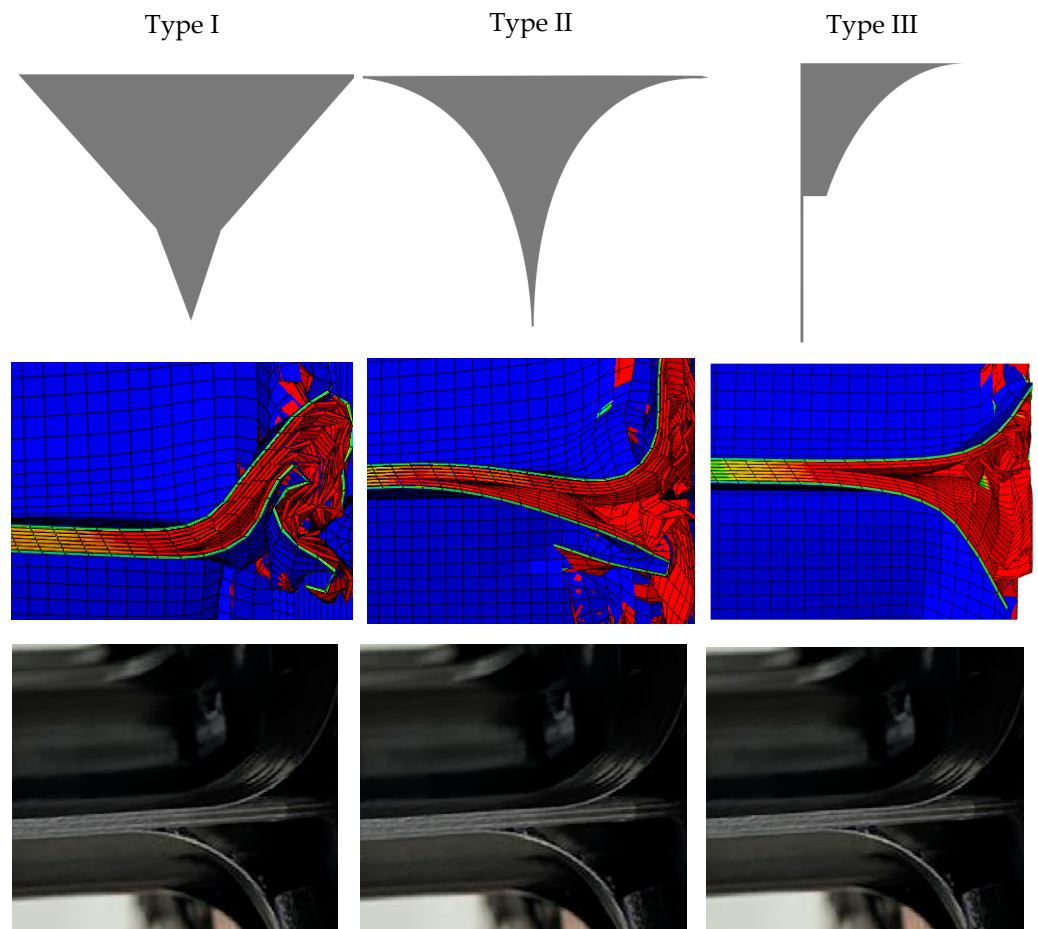


**Figure 14.** Evaluation of the artificial plug-initiator geometry and the corresponding simulation results compared with the experimentally observed failure modes.

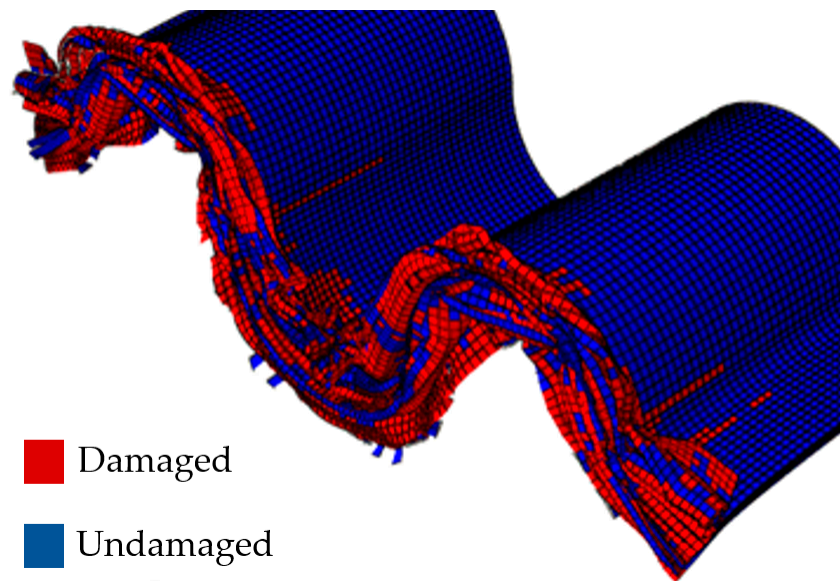


Figure 15. Simulated deformed shape of the sinusoidal specimen with an artificial plug-initiator.

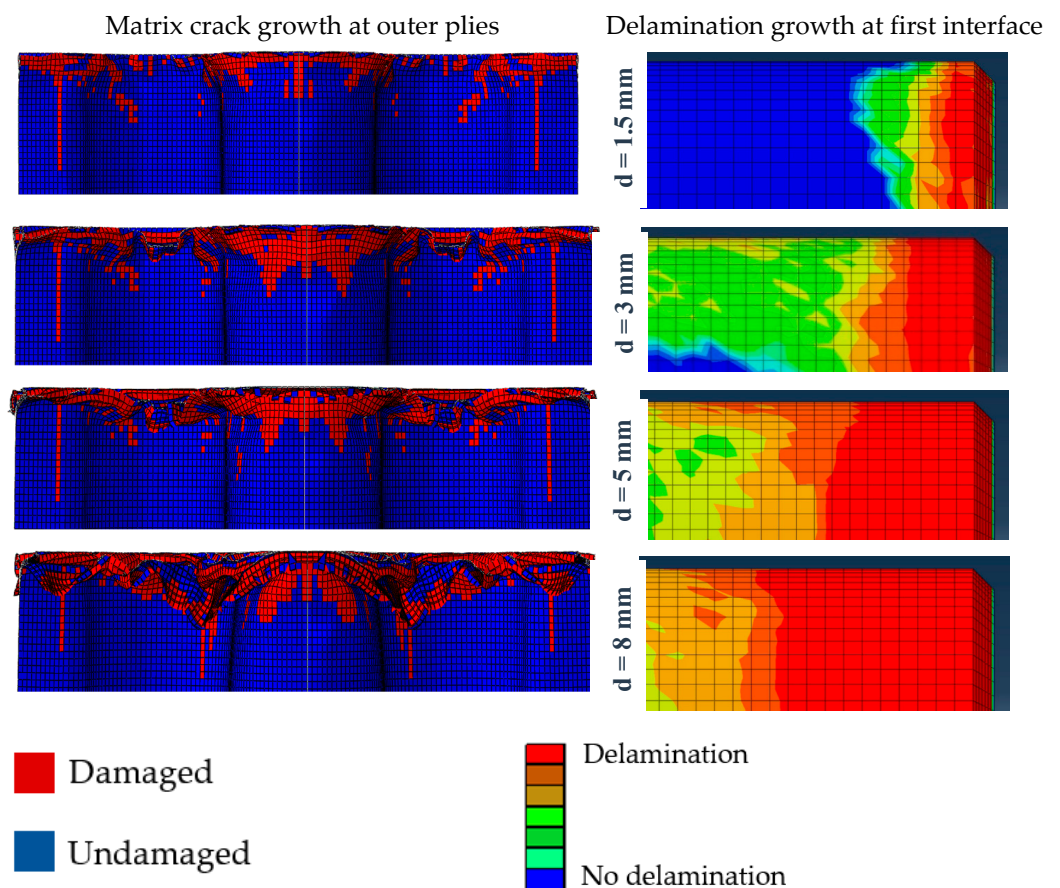
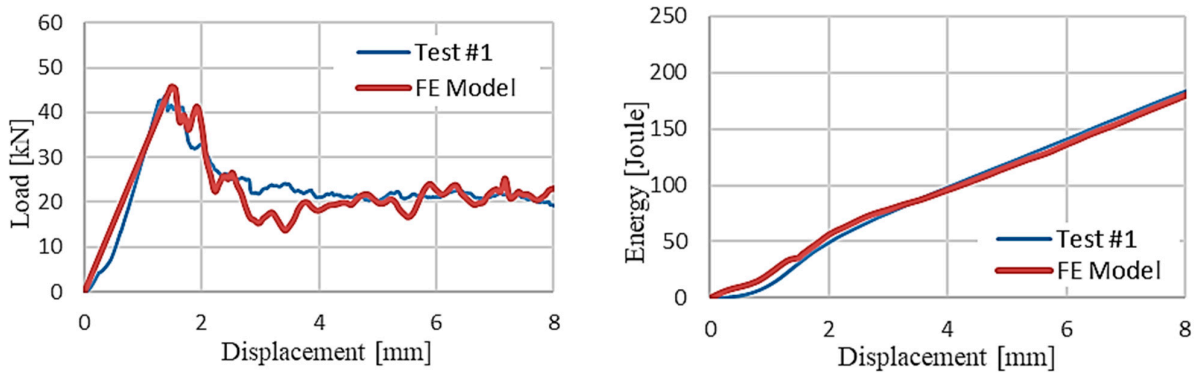


Figure 16. Matrix crack and delamination growth in the FE model with an artificial plug-initiator.

Aside from demonstrating crushing behavior correctly, the FE model with the plug-initiator estimated the amount of energy absorbed during the crush event accurately. As can be seen from Figure 17, numerical results enabled more stability in load-displacement graphs and showed good agreement with the experimental tests in terms of load-displacement and energy curves.



**Figure 17.** Comparison of the FE model (with a plug-initiator) with experimental tests: load-displacement curves (left) and energy curves (right) of the sinusoidal with 3 curvatures.

The FE model was also validated by applying the numerical analysis of the sinusoidal structure with five curvatures. According to the results given in Figure 18, numerical results had a good correlation with the experimental data. The same approach was applied for sinusoidal specimens that had seven curvatures with same properties, boundary conditions, element types, and artificial plug-initiator geometry. The results are presented in Figures 19 and 20. The specific energy absorption (SEA) value of the sinusoidal structure with seven curvatures, which is the energy obtained from the area under the load-displacement curve per crushed mass, was calculated as 66.5 J/g.

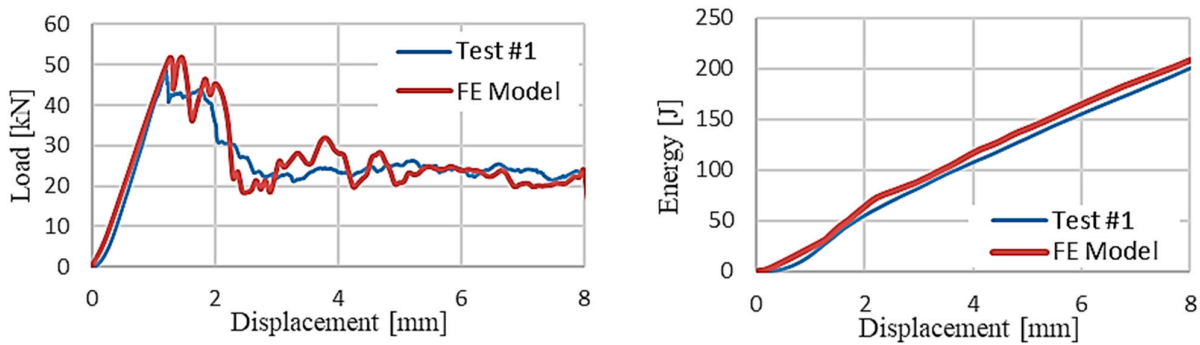


**Figure 18.** Comparison of the FE model (with a plug-initiator) with experimental tests: load-displacement curves (left) and energy curves (right) of the sinusoidal with 5 curvatures.

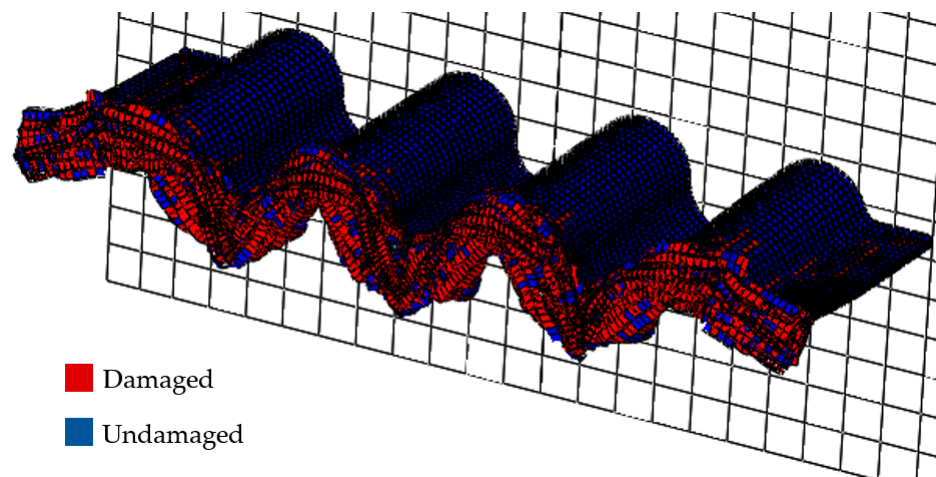


**Figure 19.** Simulated deformed shapes of the sinusoidal specimen with 7 curvatures.

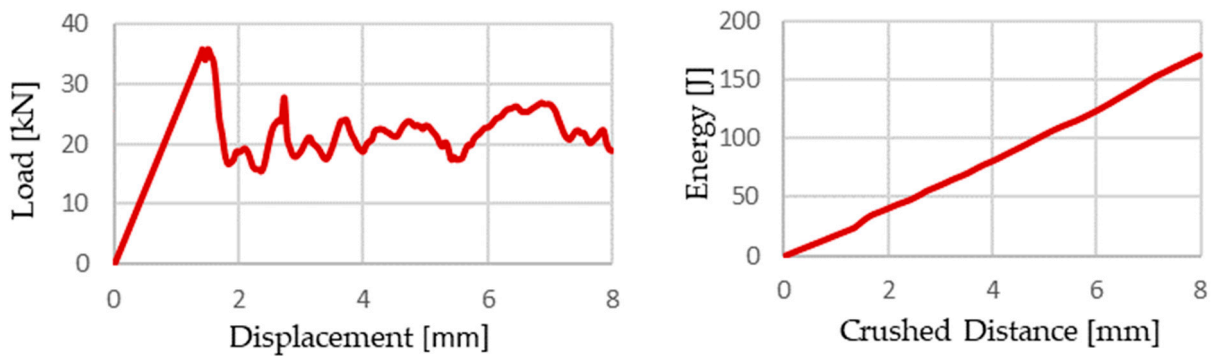


**Figure 20.** Simulation results of the sinusoidal structure with 7 curvatures: load-displacement curve (left) and energy curve (right).

Figure 21 shows the overall comparison of SEA values for various geometries, and it can be seen that the sinusoidal structure with five curvatures had the highest energy absorption capability. Beyond that structure, the performance related to energy absorption started to decrease as the number of curvatures increased. The reason behind this observation can be explained by the decrease in the aspect ratio. By decreasing the diameter of the curvatures below a certain level to increase the number of curvatures, specimen geometry converges into the flat-plate shape when its low width-to-length ratio is taken into consideration. Therefore, more instabilities occurred, and the energy absorption performance did not become better than the five-curvature specimen.

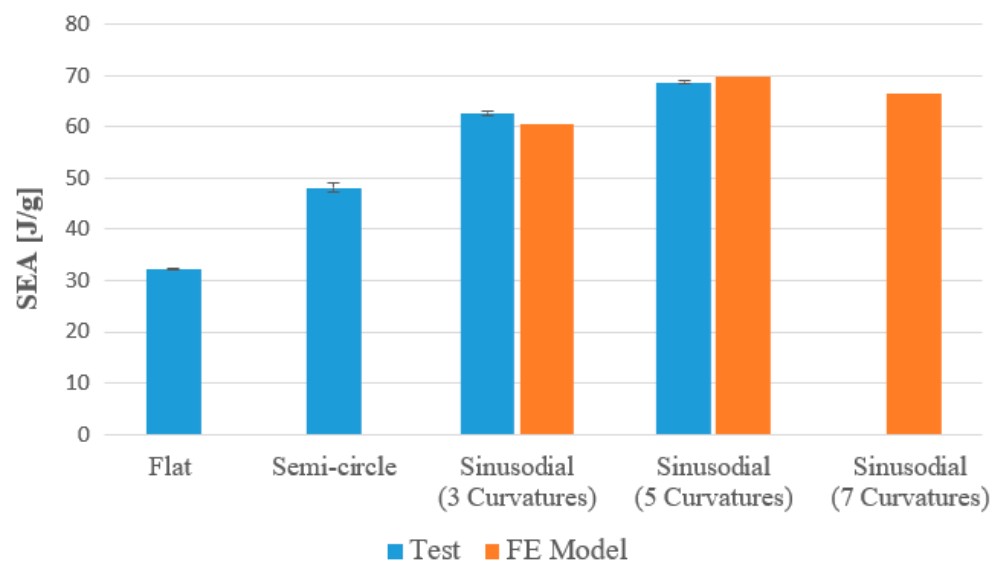


**Figure 21.** The overall comparison of SEA values from flat plates to complex structures.

### 5. Conclusions

This paper presented both experimental and numerical investigations for the crushing process of AS4/8552 carbon fiber/epoxy flat plates, semi-circle specimens, and sinusoidal structures. The main goal of this study was to understand the influence of geometry on the specific energy absorption, the variation of the crush-induced failure mechanisms through various geometries, and their contributions to the energy absorption capability.

The overall conclusion derived from the experimental study is that there is a combination of the splaying mode and the fragmentation mode, due to the matrix cracks in most of the 90-degree plies, and fiber breakages in 0-degree plies located at the center of the laminate. The levels and the occurrence rates of these failure modes apparently determines the energy absorption capability. When the crushing morphology of the semi-circle specimens

were investigated, more fragmentation was observed at the center, and vertical ruptures occurred at the outer plies, which led to a higher amount of energy absorption, compared to the flat specimens. The level of fragmentation increased even more for the sinusoidal structures, since the number of vertical ruptures increased and so did the reflection points, which connect one of the repeating semi-circle segments to another, creating obstacles that led to more micro-buckling in 0-degree plies. Therefore, sinusoidal structures have greater potential in terms of energy absorption.

The motivation behind conducting both the numerical and experimental studies for sinusoidal structures with different geometric features was to understand the reason behind the change in energy absorption capabilities and to find the structure with the better performance. The idea was to keep the amount of material (weight) constant while adding more semi-circle curvatures, which would lead to a decrease in radii. Therefore, sinusoidal structures with three, five, and seven curvatures were tested under quasi-static compression, and their energy absorption capabilities, with corresponding failure mechanisms, were discussed. The conclusion drawn from the investigation was that the sinusoidal structure with five curvatures gave the highest specific energy absorption result, due to the higher number of vertical ruptures when compared to the sinusoidal structure with three curvatures. On the other hand, for the sinusoidal structure with seven curvatures, the SEA value did not further increase because of the instabilities occurring during the crushing process related to the decreased aspect ratio (the width-to-length ratio).

One of the objectives was to develop the FE model, which can not only estimate the amount of energy absorption but also simulate the failure mechanisms occurring during the crushing process. Accurate FE models were generated in Abaqus/Explicit by including an artificial plug-initiator to obtain realistic simulation results. According to the presented results, the numerical model showed good correlation with the experimental data, was able to estimate energy absorption capability accurately, and simulated the crushing behavior consistently.

**Author Contributions:** Conceptualization, M.E.; methodology, M.E. and N.E.; validation, M.E.; investigation, M.E.; resources, N.E.; supervision, N.E. All authors have read and agreed to the published version of the manuscript.

**Funding:** This work was supported by the Boğaziçi University Research Fund, with grant number 17621D.

**Data Availability Statement:** Not applicable.

**Conflicts of Interest:** The authors declare no conflict of interest.

## References

1. Farley, G.L. Energy—Absorption Capability of Composite Tubes and Beams. Ph.D Thesis, Virginia Polytechnic Institute and State University, Hampton, VA, USA, 1989.
2. Bisagni, C. Experimental investigation of the collapse modes and energy absorption characteristics of composite tubes. *Int. J. Crashworthiness* **2009**, *14*, 365–378. [[CrossRef](#)]
3. Hull, D. A unified approach to progressive crushing of fibre-reinforced composite tubes. *Compos. Sci. Technol.* **1991**, *40*, 377–421. [[CrossRef](#)]
4. Carruthers, J.J.; Kettle, A.P.; Robinson, A.M. Energy Absorption Capability and Crashworthiness of Composite Material Structures: A Review. *Appl. Mech. Rev.* **1998**, *51*, 635–649. [[CrossRef](#)]
5. Jacob, G.C.; Fellers, J.F.; Simunovic, S.; Starbuck, J.M. Energy Absorption in Polymer Composites for Automotive Crashworthiness. *J. Compos. Mater.* **2002**, *36*, 813–850. [[CrossRef](#)]
6. Israr, H.; Rivallant, S.; Bouvet, C.; Barrau, J. Finite element simulation of 0°/90° CFRP laminated plates subjected to crushing using a free-face-crushing concept. *Compos. Part A Appl. Sci. Manuf.* **2014**, *62*, 16–25. [[CrossRef](#)]
7. Bergmann, T.; Heimbs, S. Progressive bearing failure of composites for crash energy absorption. In *Dynamic Response and Failure of Composite Materials and Structures*; Lopresto, V., Antonio, L., Serge, A., Eds.; Elsevier: Amsterdam, The Netherlands, 2017; pp. 299–334.
8. Mahdi, E.; Hamouda, M.S.; Sebaey, T.A. The effect of fiber orientation on the energy absorption capability of axially crushed composite tubes. *Mater. Des.* **2014**, *56*, 923–928. [[CrossRef](#)]
9. Hu, D.; Zhang, C.; Ma, X.; Song, B. Effect of fiber orientation on energy absorption characteristics of glass cloth/epoxy composite tubes under axial quasi-static and impact crushing condition. *Compos. Part A Appl. Sci. Manuf.* **2016**, *90*, 489–501. [[CrossRef](#)]

10. Sivagurunathan, R.; Way, S.L.T.; Sivagurunathan, L.; Yaakob, M.Y. The Effects of Triggering Mechanisms on the Energy Absorption Capability of Circular Jute/Epoxy Composite Tubes under Quasi-Static Axial Loading. *J. Reinf. Plast. Compos.* **2018**, *37*, 824–840. [[CrossRef](#)]
11. Jiménez, M.; Miravete, A.; Larrodé, E.; Revuelta, D. Effect of trigger geometry on energy absorption in composite profiles. *Compos. Struct.* **2000**, *48*, 107–111. [[CrossRef](#)]
12. Sawamura, S.; Yamazaki, Y.; Yoneyama, S.; Koyanagi, Y. Multi-scale numerical simulation of impact failure for cylindrical CRFP. *Adv. Compos. Mater.* **2021**, *30*, 19–38. [[CrossRef](#)]
13. Feraboli, P. Development of a Modified Flat-plate Test Specimen and Fixture for Composite Materials Crush Energy Absorption. *J. Compos. Mater.* **2009**, *43*, 1967–1990. [[CrossRef](#)]
14. Bru, T.; Walderström, P.; Gutkin, R.; Vyas, G.M. Development of a Test Method for Evaluating the Crushing Behaviour of Unidirectional Laminates. *J. Compos. Mater.* **2017**, *57*, 1–11. [[CrossRef](#)]
15. Thornton, P. Energy Absorption in Composite Structures. *J. Compos. Mater.* **1979**, *13*, 248–262. [[CrossRef](#)]
16. Mamalis, A.; Robinson, M.; Manolakos, D.; Demosthenous, G.; Ionnidis, M.; Carruthers, J. Review: Crashworthy capability of composite material structures. *Compos. Struct.* **1997**, *37*, 109–134. [[CrossRef](#)]
17. Farley, G.L.; Jones, R.M. Crushing Characteristics of Composite Tubes with “Near-Elliptical” Cross Sections. *J. Compos. Mater.* **1992**, *26*, 1741–1751. [[CrossRef](#)]
18. Alhyari, O.; Newaz, G. Energy Absorption in Carbon Fiber Composites with Holes. *J. Carbon Res.* **2021**, *7*, 16. [[CrossRef](#)]
19. Hanagud, S.; Craig, I.; Sriram, P.; Zhou, W. Energy Absorption Behavior of Graphite Epoxy Composite Sine Webs. *J. Compos. Mater.* **1989**, *23*, 448–459. [[CrossRef](#)]
20. Wiggenraad, J.F.M.; Santoro, D.; Lepage, F.; Kindervater, C.; Mañez, H.C. Development of a crashworthy composite fuselage concept for a commuter aircraft. *NLR-TP* **2001**, *108*, 11.
21. Sokolinsky, V.S.; Indermuehle, K.C.; Hurtado, J.A. Numerical simulation of the crushing process of a corrugated composite plate. *Compos. Part A Appl. Sci. Manuf.* **2013**, *42*, 1119–1126. [[CrossRef](#)]
22. Hexcel. *HexPly®8552—Product Data Sheet*; EU Version; Hexcel: Stamford, CT, USA, 2016.
23. Hashin, Z. Failure criteria for unidirectional fibre composites. *J. Appl. Mech.* **1980**, *47*, 329–334. [[CrossRef](#)]
24. Lubineau, G. On a damage mesomodel for laminates: Micro–meso relationships, possibilities, and limits. *Comp. Sci. Technol.* **2001**, *15*, 2149–2158.
25. Camanho, P.P.; Davila, G.G.; Moura, M.F. Numerical simulation of mixed-mode progressive delamination in composite. *Mater. Sci. Compos.* **2003**, *16*, 1415–1438. [[CrossRef](#)]
26. Turon, A.; Dávila, C.; Camanho, P.; Costa, J. An engineering solution for mesh size effects in the simulation of delamination using cohesive zone models. *Eng. Fract. Mech.* **2007**, *74*, 1665–1682. [[CrossRef](#)]
27. Oz, F.E.; Ahmadvashghbash, S.; Ersoy, N. Damage mode identification in transverse crack tension specimens using acoustic emission and correlation with finite element progressive damage model. *Compos. Part B Eng.* **2019**, *165*, 84–95. [[CrossRef](#)]
28. Oz, F.E.; Calik, E.; Ersoy, N. Finite element analysis and acoustic emission monitoring of progressive failure of corrugated core composite structures. *Compos. Struct.* **2020**, *253*, 112775. [[CrossRef](#)]
29. Ahmadvashghbash, S.; Engül, M.; Öz, F.E.; Ersoy, N. A Comparative Numerical Study Aiming to Reduce Computation Cost for Mode-I Delamination Simulations. In Proceedings of the ECCM-18, Athens, Greece, 24–28 June 2018.
30. ABAQUS. *Standard User’s Manual*; Version 6.14; Dassault Systemes Simulia, Inc.: Johnston, RI, USA, 2014.

**Disclaimer/Publisher’s Note:** The statements, opinions and data contained in all publications are solely those of the individual author(s) and contributor(s) and not of MDPI and/or the editor(s). MDPI and/or the editor(s) disclaim responsibility for any injury to people or property resulting from any ideas, methods, instructions or products referred to in the content.